12-2016

# Remote sensing of snow using bistatic radar reflectometry

Abi Komanduru
*Purdue University*

# REMOTE SENSING OF SNOW USING BISTATIC RADAR REFLECTOMETRY

by

**Abi Komanduru**

**A Thesis**

*Submitted to the Faculty of Purdue University*

*In Partial Fulfillment of the Requirements for the degree of*

**Master of Science in Aeronautics and Astronautics**

Department of Aeronautics and Astronautics

West Lafayette, Indiana

December 2016

# THE PURDUE UNIVERSITY GRADUATE SCHOOL
# STATEMENT OF THESIS APPROVAL

Dr. James Garrison, Chair

Department of Aeronautics and Astronautics

Dr. Arthur Frazho

Department of Aeronautics and Astronautics

Dr. Rashmi Shah

NASA JPL/Caltech

**Approved by:**

Dr. Weinong Chen

Head of the Departmental Graduate Program

*To my family and friends*

# ACKNOWLEDGMENTS

This research was funded by the Jet Propulsion Laboratory (JPL) Research and Technology Development (R&TD) Award, subcontract number 1514746, to Prof. James L Garrison, entitled "Multi-Frequency Bistatic Reflectometry Using Signals of Opportunity (SoOps)”.  We would like to acknowledge Dr. Kelly Elder of the United States Forest Service for providing access to the Frasier Experimental Forest and assisting us in the collection and understanding of in situ snow data.

# TABLE OF CONTENTS

# LIST OF TABLES

# LIST OF FIGURES

.

# ABSTRACT

Author: Komanduru, Abi, C. MSAAE
Institution: Purdue University
Degree Received: December 2016
Title: Remote Sensing of Snow using Bistatic Radar Reflectometry.
Major Professor: James Garrison

Snow and ice processes are a critical part of the Earth's hydrological and climate cycles. These processes can serve as an important source of fresh water as well as a cause of flooding. Various missions have been proposed by NASA and ESA for the purpose of remote sensing of snow. This research looks at applying bistatic radar reflectometry to the remote sensing of snow water equivalent. The resulting phase offset from changes in optical path length due to reflection through snow are the primary measurements made. The research uses data from a field campaign in Fraser, CO, involving an instrument collecting direct and reflected from S band during Jan 2015 – Apr 2015. Phase measurements from the field data are made from the two signals and compared to theoretical phase computed from a forward model using in-situ data. A moderate correlation (>0.6) is found between the measured and modeled phase.

# 1. INTRODUCTION

## 1.1 Introduction

Snow and ice processes play an important role in the Earth's hydrological and climate cycles. These processes range from highly dynamic seasonal snowfall, melting and refreezing to slow evolving terrestrial snow and ice cover [1]. Additionally snow processes can serve as a significant source of fresh water in some regions. Although in-situ methods of measuring snow and ice parameters have been established, the nature of these processes and the locations in which they occur may make it infeasible to regularly collect accurate data using these methods. This thesis looks at applying bistatic radar remote sensing for collecting snow and ice data. Bistatic radar remote sensing provides the advantage of requiring only a local receiver for a single existing transmitter. In addition to reduced costs in instrument construction from lack of transmitter, the reduced size and weight of the resulting instruments based on this method results in a relatively portable design. Other applications of this method include use of GNSS (Global Navigation Satellite System) signals for ocean remote sensing [2].

## 1.2 History of Snow Remote Sensing

NASA has recommended and deployed various missions looking into snow and cold land processes including SMAP (Freeze thaw cycles), SCLP and CoReH2O in its 2007 decadal survey [3]. Existing research has looked at the concept of retrieving snow and ice parameters using various remote sensing techniques including Terrestrial Laser Scanning and Synthetic Aperture Radar (SAR) interferometry [4]. This method provides the advantage of being able to retrieve snow parameters even during hazardous conditions which may discourage in situ measurements. The process of retrieving snow and ice parameters from radar backscatter has been previously used in mission proposals such as the Cold Region Hydrology High-resolution Observatory (CoReH2O), which proposed using X-band and Ku-band backscatter measurements to make SAR satellite measurements of snow water equivalent (SWE) and winter snow accumulation on glaciers [5]. The phase change observed through reflectometry overtime can be shown to be a function of SWE and independent of snow grain size and snow density [6]. Previous research has looked at SWE retrieval using microwave radiometry under dry snow conditions [7] as well as looking at dry snow using GNSS interferometric reflectometry (GPS-IR) [8]. GPS reflectometry has also been used in the remote sensing of soil moisture and water content in vegetation [9]. GPS-IR has also been used to determine snow depth and SWE in the United States [10] [11]. This is done by looking at fringes that are formed in SNR (Signal-Noise Ratio) timeseries from the interference of the direct and reflected signal recorded by stationary GPS antennas. The experiment discussed in this thesis uses S-band reflectometry to measure optical path length changes due to snow and relate them to changes in SWE. Optical path length changes due to the presence of snow are measured in the form of phase changes and are compared to phase changes predicted by a forward model based on in-situ SWE measurements.

# 2. SCIENTIFIC THEORY

## 2.1 Fundamental Principles

The fundamental principle behind the remote sensing of snow through reflectometry is the comparison of the signals that have been reflected off of snow (reflected signals) to signals directly from the satellite (direct signals). To apply this method, the following assumptions have been made:

1. The reflection is specular.
2. The reflected signal is dominated by reflection off a snow-soil boundary or, if present, a snow-ice boundary, i.e. scattering from the snow is negligible [12].
3. The snowpack is dry. If the snow pack is wet, the penetration depth of the signals used are significantly reduced [13].
4. The effect of reflection by snow is the change in optical path length(represented by delay in time, $\tau$) and the change in power of the received signal(represented by a reflection coefficient $r$)

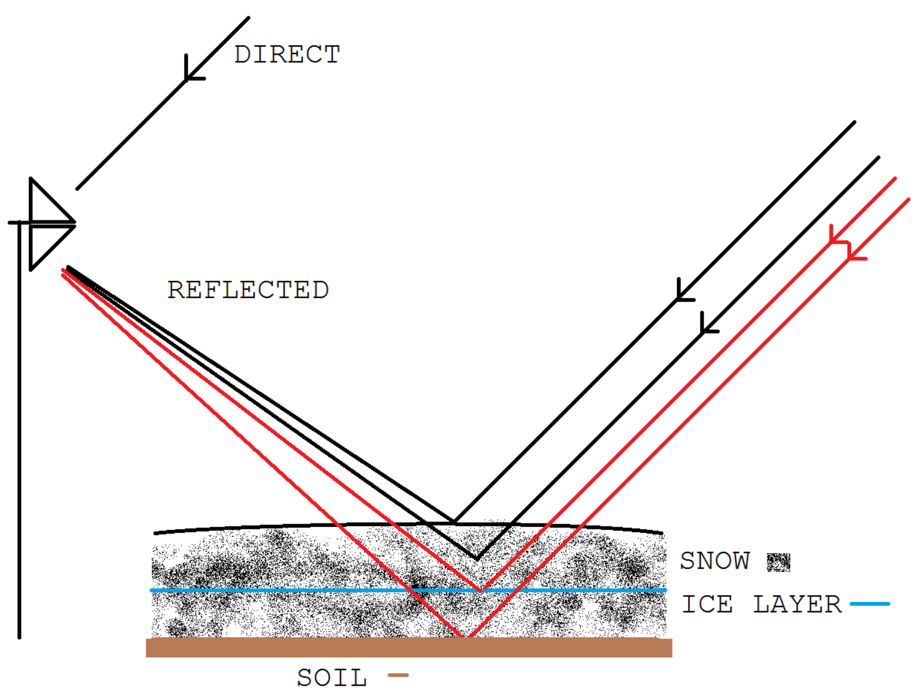


Figure 2.1 Reflection of Signal off Snow, Soil and Ice

A simple, ideal mathematical model for this would be as follows. If

$$X_d = X(t)e^{i\omega_c t}$$

is the direct signal, where $X(t)$ is the modulated information timeseries and $\omega_c = 2\pi f_c$ is the carrier frequency in cycles/sec. Then the reflected signal is

$$X_r(t) = X(t-\tau)e^{i\omega_c(t-\tau)}$$

Information of the Air-Snow-Soil system, in particular about snow depth and density can be obtained by looking at the change in optical path length. With an 8MHz sampling rate the resolution of the optical path length difference that can be measured through looking at the magnitude of the cross correlation is the path difference between two successive samples

$$\Delta l = \frac{c}{8 \times 10^6 Hz} = 37.47\ m$$

This resolution is not good enough to observe small changes in SWE and snow depth. Instead we look at the phase difference between the direct and reflected signal. In this case, a difference of one cycle corresponds to an optical path difference up to

$$\Delta l = \frac{c}{2.345 \times 10^9 Hz} = 0.12\ cm$$

While this is a significantly better resolution, this method is limited by the fact that it is difficult to distinguish changes greater than one cycle in magnitude, i.e. the phases must be unwrapped. Furthermore, it can be shown that the phase measured depends only on SWE and not on other snow parameters such as snow grain size or density [6].

### 2.2 Computing Change in Optical Path Length from Reflection off Air-Snow-Soil System

Given the ideal model of the received signals from 2.1, methods of estimating the parameters $r, \tau$ can be discussed. Assuming that the recording instrument does not attenuate the received signals and only shifts them to an intermediate frequency, consider the following forms for the direct and reflected signals.

$$X_d(t) = X(t)e^{i\omega_i t}$$

$$X_r(t) = rX(t-\tau)\ e^{i\omega_i(t-\tau)}$$

Where $X(t)$ is the baseband signal, $\omega_i$ is the intermediate frequency and $\tau = \frac{\phi}{\omega_c}$ is the delay in the reflected signal with a corresponding phase $\phi$. In the case of received communication signals, the finite length signals recorded are part of a continuously transmitted infinite length signal. Thus we can use the circular correlation of two signals of length N each, defined as

$$(X \star Y)_N(k) = \sum_{n=0}^{N} X^*(n)Y\big((n+k)modN\big)$$

Given continuous signals we can sample uniformly at a sampling frequency $f_s$ to convert to discrete time. Circular correlation is also equivalent to multiplication in the frequency domain. If we now consider the circular correlation of the two signals (represented here by the operation ($\star$), we find that the circular cross correlation of the direct and reflected signals is given by

$$X_d(t) \star X_r(t) = \mathcal{F}^{-1}\{\mathcal{F}\{X_d(t)\}\mathcal{F}\{X_r(t)\}^\star\}$$
$$= \mathcal{F}^{-1}\left\{\hat{X}(\omega - \omega_i)\left(\hat{X}(\omega - \omega_i)e^{-\frac{j\omega\phi}{\omega_c}}\right)^\star\right\}$$

Where $\hat{Y} = \mathcal{F}\{Y(t)\}$ represents the Fourier transformation. Taking the Fourier Transform on both sides we get

$$\mathcal{F}\{X_d(t) \star X_r(t)\} = \hat{X}(\omega)\left(\hat{X}(\omega)e^{-\frac{j\omega\phi}{\omega_c}}\right)^\star = \hat{X}(\omega)\hat{X}^*(\omega)e^{\frac{j\omega\phi}{\omega_c}}$$

$$\Rightarrow \angle(\mathcal{F}\{X_d(t) \star X_r(t)\}) = \frac{\omega\phi}{\omega_c}$$

Let $\gamma(\omega) = \angle(\mathcal{F}\{X_d(t) \star X_r(t)\})$, then

$$\phi = \underset{\theta}{\operatorname{argmin}} \left|\gamma(\omega) - \frac{\theta\omega}{\omega_c}\right|, \omega \in B$$

Where $B$ is the frequency region of the signal.

$$B = \left[\omega_0 - \frac{b}{2}, \omega_0 + \frac{b}{2}\right]$$

Where $\omega_0$ is the carrier frequency of the signal at baseband and $b$ is the bandwidth of the signal.

Thus the phase can be obtained by solving the least squares minimization problem presented above.

### 2.3 Computing Reflectivity of Air-Snow-Soil System

The reflectivity can be retrieved by correlation of the received signals.

again, let $X_d(t) = X(t)e^{i\omega_i t}, X_r(t) = rX(t-\tau)\ e^{i\omega_i(t-\tau)}$ be the idealized direct and reflected signals respectively. We have

$$R_d(t) = X_d(t) \star X_d(t) = (X \star X)(t)$$

$$R_r(t) = X_r(t) \star X_r(t) = r(X \star X)(t-\tau)$$

Where the $\star$ represents the circular correlation operation.

Using the above $r$ can be estimated by the ratio of $R_R(\tau)$ to $R_d(0)$

$$r^2 = \frac{R_r(0)}{R_d(0)} = \left(\frac{\chi_{dr}(\tau)}{R_d(0)}\right)^2$$

This is a known result for power signals.

In reality there is a noise term (represented here by $N$)

$$X_d(t) = X(t)e^{i\omega_i t} + N_1(t), X_r(t) = rX(t-\tau)e^{i\omega_i(t-\tau)} + N_2(t)$$

These noises are finite length so the variance of the autocorrelation of the noise is non-zero far from the zero lag. We now have

$$\begin{aligned} R_d(t) &= X_d(t) \star X_d(t) \\ &= X(t) \star X(t) + X(t)e^{i\omega_i t} \star N_1(t) + N_1(t) \star X(t)e^{i\omega_i t} + N_1(t) \star N_1(t) \end{aligned}$$

$$\begin{aligned} R_r(t) &= X_r(t) \star X_r(t) \\ &= r^2\big(X(t) \star X(t)\big) \\ &\quad + r\big(X(t-\tau)e^{i\omega_i(t-\tau)} \star N_2(t) + N_2(t) \star X(t-\tau)e^{i\omega_i(t-\tau)}\big) + N_2(t) \\ &\quad \star N_2(t) \end{aligned}$$

$$\begin{aligned} \mathrm{R_{dr}}(t) &= X_d(t) \star X_r(t) \\ &= rR_d(t-\tau) + X(t)e^{i\omega_i t} \star N_2(t) + rN_1(t) \star X(t-\tau)e^{i\omega_i(t-\tau)} + N_2(t) \\ &\quad \star N_2(t) \end{aligned}$$

In each of the case we assume that the $X(t) \star N(t)$ and $N(t) \star X(t)$ are zero and eliminate the effect of the $N_i(t) \star N_j(t)$ term by subtracting the variance far from the peak.

## 2.4 S-band Signal Structure

The signals used to perform S-band measurements is from existing XM satellites. XM is a Satellite Digital Audio Radio Service (SDARDS) operated by Sirius XM Radio in the S Band from 2320 to 2345 MHz. The currently active system includes two satellites “Rhythm” and “Blues” in addition to terrestrial repeaters across North America. The details of the Satellites can be found in Table 2-1 [14] [15]. The signal occupies a spectrum allocation in the S Band with a total of four carriers (2 per satellite) as shown in Figure 2.2. The downlink signals are LHCP (Left Hand Circular Polarization) and uplink signals are RHCP (Right Hand Circular Polarization). The modulation used is QPSK (Quadrature Phase Shift Keying) with a symbol rate of 1.64Msps [16]. For the purpose of this experiment, it is assumed that the binary data transmitted is random with a uniform distribution.

Table 2-1 XM Satellites [17]

| **Satellite** | **XM-3** | **XM-4** |
|---|---|---|
| **Name** | Rhythm | Blues |
| **Frequencies** | 2333.47MHz, 2344.05MHz | 2335.31MHz, 2342.21MHz |
| **Longitude** | $85.1^0$W | $115.0^0$W |

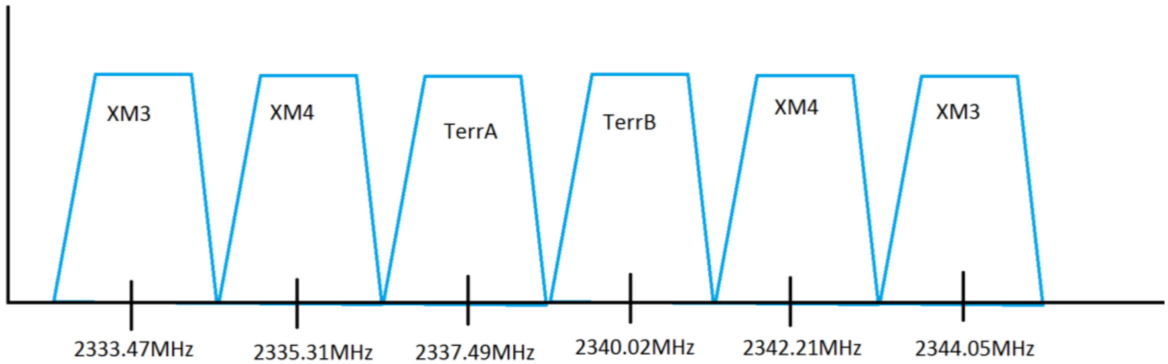


Figure 2.2 XM Spectrum [14]

In the figure shown above the bands broadcasted by “Rhythm” and “Blues” can each be seen at two different frequencies. Each satellite broadcasts a signal with bandwidth 1.866MHz. In this experiment, only the two upper bands centered at 2.342205 GHz and 2.34405 GHz are recorded. An example of the resulting power spectral density made using data collected along with a Levinson filter can be seen in Figure 2.3.

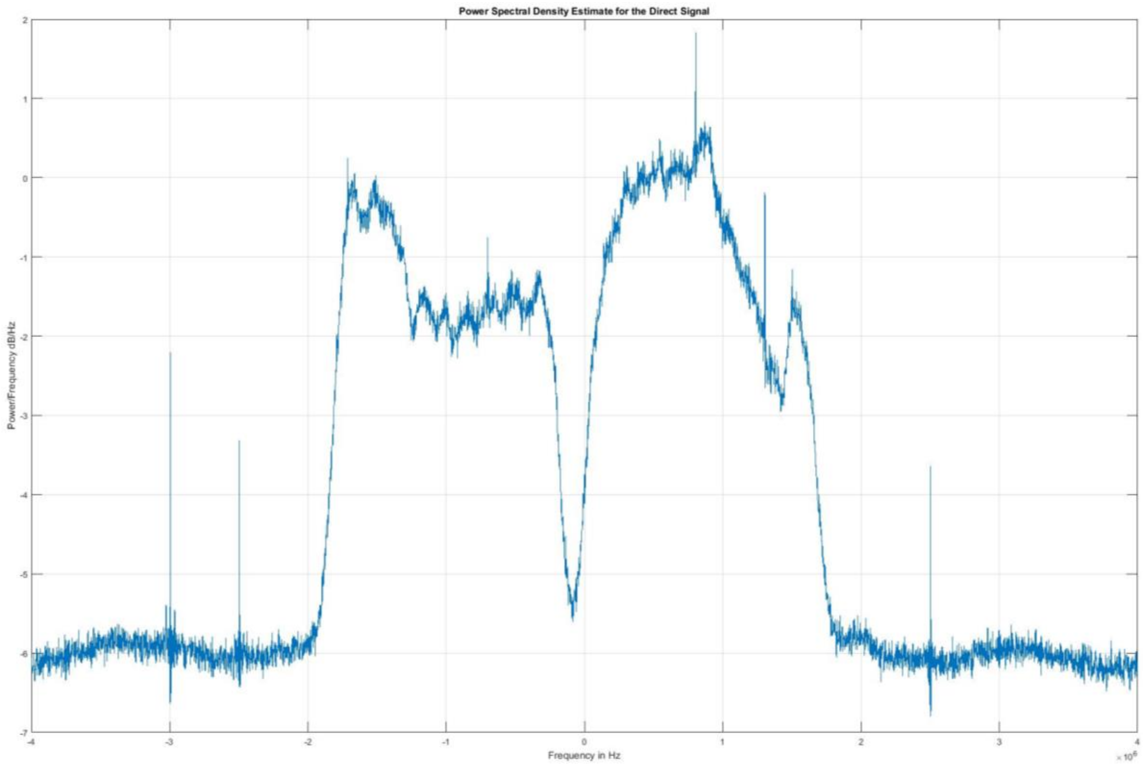


Figure 2.3 Power Spectral Density Estimate of Direct signal

As can be seen, part of the repeater band is also recorded. Since there are no repeaters in the experiment site of Fraser, CO, this band should contain only noise.

## 2.5 Phase Averaging and Circular Mean

One of the methods of removing zero mean white noise is averaging. However, to average phase during phase retrieval for the purpose of noise removal and during the transfer switched based calibration method a small adjustment must be made. For example, the average of $-\pi$ and $\pi$ is 0 but when looking at phases the average should be $\pi$ which can be seen when plotted on the unit circle. To fix this, we use a wrapped normal distribution [18]. The (circular) mean of set $\{\phi_n\}$ is given by

$$\bar{\phi} = \angle(\bar{z}) = \angle\left(\frac{1}{\mathrm{N}}\Sigma e^{i\phi_n}\right)$$

This is the mean that is used in this experiment for averaging phase.

The corresponding standard deviation is given by:

$$\sigma = \sqrt{\ln\left(\frac{1}{R^2}\right)}$$

Where $R = |\bar{z}|^2$

# 3. EXPERIMENT

## 3.1 Implementation

To record and compare phase from signal reflected off of snow and compare it to SWE, a receiver system had to be designed and deployed along with simultaneous in-situ measurements of the relevant snow parameters. One of the major considerations for the experiment design was the difference in channels that the direct and reflected signals were recorded through. Since these channels contained different amplifiers and long cables connecting them to the SDR (Software Defined Radio), it was necessary to implement a method of calibrating out these differences. This was done through two methods: (1) using a splitter to pass the direct signal through both channels, and (2) using a transfer switch so that the channels used direct and reflected signals are swapped. While method (1) is straightforward, method (2) is discussed in detail in the following section.

## 3.2 Calibration of system

Assume channel A and B delay the signal by $\tau_A$ and $\tau_B$ and change the phase of the signal by $\phi_A$ and $\phi_B$ and the amplitude by $A_A$ and $A_B$ respectively through the presence of amplifiers and other RF (Radio Frequency) components. Calibration of the two channels is done through the following methods:

### 3.2.1 Using Splitter


Figure 3.1 Splitter method of calibration

In this calibration method, the signal from the sky-view antenna is sent through a splitter and through both channels used normally by the sky-view and ground view antenna. The data is then recorded and calibrated. Assume a signal $X(t)$ that is split up and passed through both channels with equal power. Neglecting noise, we have

$$X_A(t) = A_A X(t - \tau_A) e^{i\phi_A}$$
$$X_B(t) = A_B x(t - \tau_B) e^{i\phi_B}$$

Taking the Fourier transform of the two signal we have

$$\hat{X}_A(\omega) = A_A X(\omega) e^{i(\phi_A - \tau_A)}$$
$$\hat{X}_B(\omega) = A_B X(\omega) e^{i(\phi_B - \tau_B)}$$

So now we have

$$\frac{|X_A(t) \star X_B(t)|_{t=t_{max}}}{|X_A(0) \star X_A(0)|} = \frac{A_A}{A_B}$$
$$\angle\left(\hat{X}_A(\omega)\hat{X}_B^*(\omega)\right) = \phi_A - \tau_A - (\phi_B - \tau_B)$$

### 3.2.2 Using Transfer Switch

In this method of calibration, after normal data collection using both the skyview and the earthview antennas, the channels and amplifiers used by the two signals are exchanged using a transfer switch. The gains along both paths after the transfer switch are calibrated using the following method:

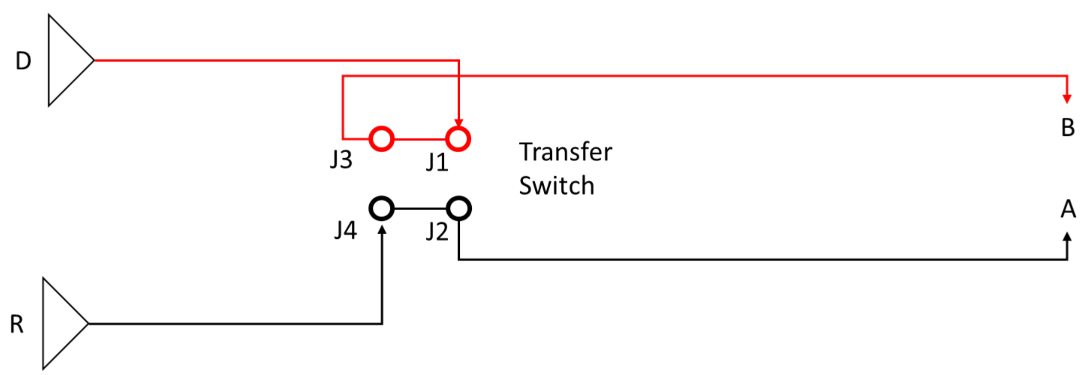


Figure 3.2 Transfer switch off configuration

**<u>Transfer Switch off:</u>** Let the skyview antenna be connected to channel B and the earth view antenna be connected to channel A. Again neglecting noise we have:

$$X_A(t) = A_A X_R(t-\tau_A)e^{i\phi_A} = A_A r X(t-\tau-\tau_A)e^{i\phi_A}$$
$$X_B(t) = A_B X_D(t-\tau_B)e^{i\phi_B} = A_B r X(t-\tau_B)e^{i\phi_B}$$

Again taking the Fourier transform we get

$$\hat{X}_A(\omega) = A_A r \hat{X}(\omega)e^{i(\phi_A-\omega\tau-\omega\tau_A)}$$
$$\hat{X}_B(\omega) = A_B \hat{X}(\omega)e^{i(\phi_B-\omega\tau_B)}$$
$$r_0 = \frac{|X_A(t)\star X_B(t)|_{t=t_{max}}}{|X_B(0)\star X_B(0)|} = \frac{A_A}{A_B}r$$
$$\phi_0 = \angle\left(\hat{X}_A(\omega)\hat{X}_B^*(\omega)\right) = \phi_A - \omega\tau - \omega\tau_A - (\phi_B - \omega\tau_B)$$

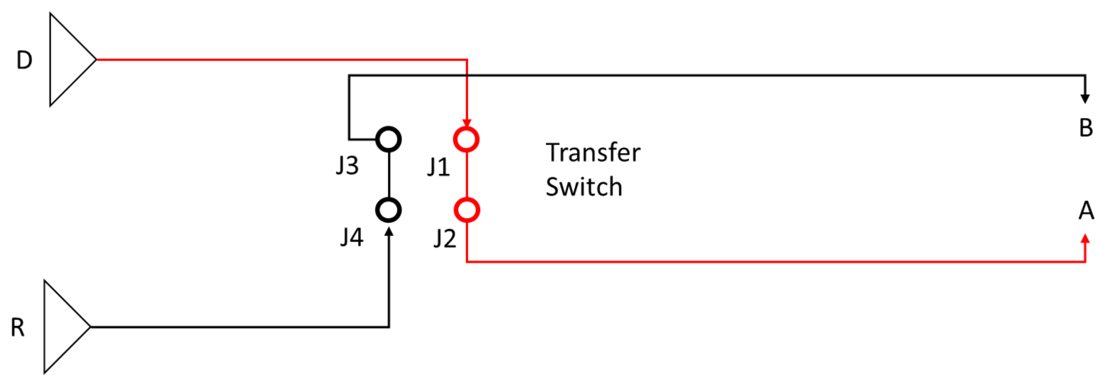


Figure 3.3 Transfer switch on configuration

**Transfer Switch On:** When the transfer switch is activated the signals change as follows

$$X_A(t)_T = A_A X_D(t-\tau_A)e^{i\phi_A} = A_A X(t-\tau_A)e^{i\phi_A}$$
$$X_B(t)_T = A_B X_R(t-\tau_B)e^{i\phi_B} = A_B r X(t-\tau-\tau_B)e^{i\phi_B}$$

$$X_A(\omega)_T = A_A X(\omega)e^{i(\phi_A-\omega\tau_A)}$$
$$X_B(\omega)_T = A_B r X(\omega)e^{i(\phi_B-\omega\tau-\omega\tau_B)}$$
$$r_T = \left.\frac{|X_A(t)\star X_B(t)|_{t=t_{max}}}{|X_A(0)\star X_A(0)|}\right|_T = \frac{A_B}{A_A}r$$
$$\phi_T = \angle\left(\hat{X}_A(\omega)\hat{X}_B^*(\omega)\right)_T = \phi_A - \omega\tau_A - (\phi_B - \omega\tau - \omega\tau_B)$$

Using both the results we are able to eliminate the gains, delay and the phase shift from both the channels and retrieve only the phase and reflection coefficient required.

$$r = \sqrt{r_0 r_T}$$

$$\phi = mean(\phi_0, \phi_T)$$

.

These methods enable calibration of the phase and amplitude differences from the path of the signals after the transfer switch when determining change in amplitude/phase from reflection. They also serve as a measure of stability of the amplifier as changes in the amplifiers over time would show up in the calibration measurements. The design of the receiver instrument is driven primarily by the calibration requirement. The next section discusses the design of the instrument used in this experiment.

### 3.3 Receiver Design

The receivers built used the architecture as shown in Figure 3.4. The setup for each system involves three antennas: a sky-view antenna, a co-pole earth-view antenna and a cross pole earth-view antenna connected to a receiver system which fed into a recording computer through an SDR. The S-band system used a LHCP for the sky-view antenna while the P-band system uses RHCP antennas. The antennas used for the S-band system are Antcom 3M23L-A-XT2 [19] for LHCP and Antcom 3M23R-A-XT2 [19] for RHCP, while the P-band system (see APPENDIX A1) uses homebrew Yagi antennas. These antennas were on top of a portable tower and were connected to a receiver system located just below.

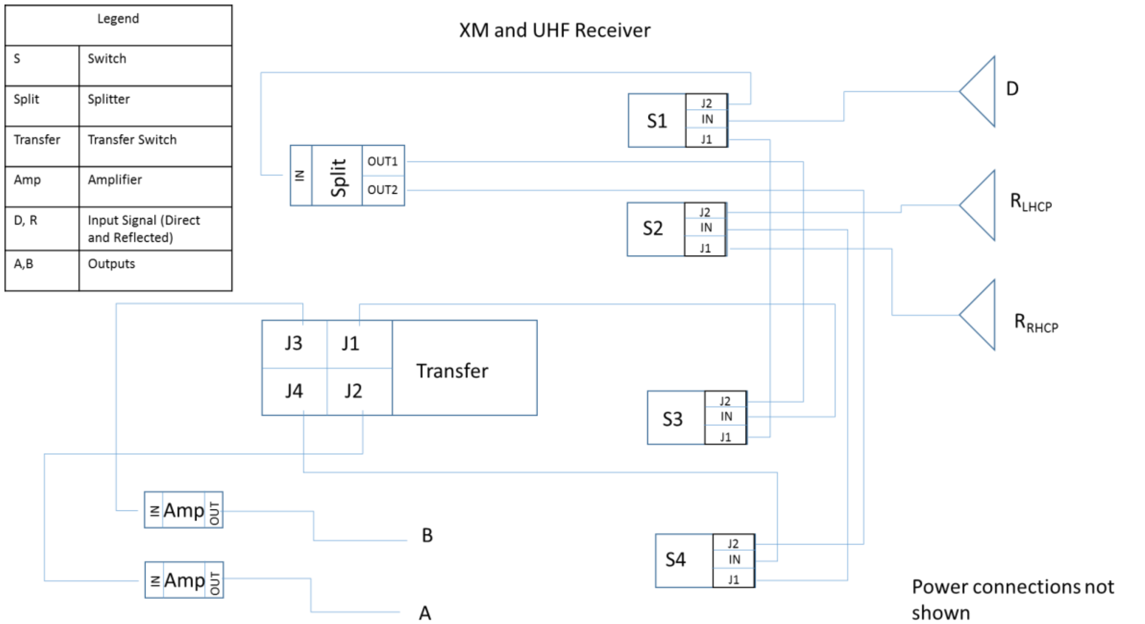


Figure 3.4 Schematic of Receiver System

The receiver system as shown in Figure 3.4 comprises of two amplifiers, a transfer switch and an arrangement of switches that can be toggled through a relay to select which antennas to use along two different channels which lead to two output ports. The switches can also be toggled to enable calibration of both channels through either sending the signal from a single antenna (the sky-view antenna) through a splitter and down both of the channels. Alternatively a secondary method of calibration can be engaged through a transfer switch which exchanges the channels travelled by the signals from the two selected antennas. This allows for two independent methods of calibrating the amplifier gains along the two channels to the output.

The two outputs are connected to two ports of a USRP B210 SDR [20] which is located at the bottom of the portable tower. The entire system is controlled by a computer running Ubuntu Linux. The USRP converts the signals from the two channels to baseband using a 2.3432GHz center frequency and samples the signals at a sampling rate of 8MHz with 8 bit quantization. The samples are then sent to the controlling computer via USB where they are recorded. The final set up on the tower at Fraser, CO can be seen in Figure 3.6.

## 3.4 Experimental Campaign in Fraser CO

The experiment campaign used to acquire the data for this project involved setting up a receiver system for both S-band and P-band in Fraser, CO. The deployed setup can be seen in Figure 3.6. In-situ measurements of snow depth were made through a snow pit on site. Additionally, SWE and air temperature data was obtained from in-situ measurements made by the US Forest Service at Fraser. Snow depth measured during the campaign is shown in Figure 3.5.

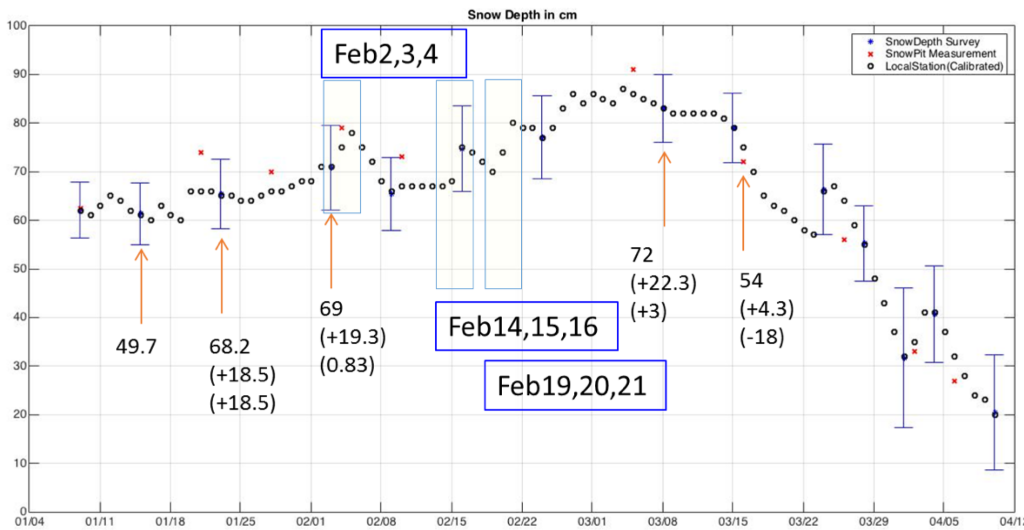


Figure 3.5 Snow depth change during experiment

Figure 3.6 Set up at Fraser CO

The setup resulted in two distinct specular points for XM3 and XM4 which were located at approximately 40m, $150^0$ clockwise from true north and 35m, $194^0$ clockwise from true north with respect to the base of the tower. A distance of about 35m separated the two specular points.

### 3.4.1 Data Collection

Reflectometry measurements were made in Fraser, CO from Jan 26, 2015 to April 4, 2015. The major data collection parameters can be found in Table 3-1.

Table 3-1: Data Collection Parameters

| Parameter | Value | Comments |
|---|---|---|
| **Center Frequency** | 2343.2 MHz | |
| **Sampling Rate** | 8 MHz | |
| **Collection Modes** | RHCP, RHCP+TS, Splitter, Splitter+TS | LHCP and LHCP+TS failed to be collected |
| **Collection Rate** | 2 min per 3 hour (for each Mode) | Collected in 2 sec bursts |
| **Data Format** | 16 bit Short Complex | |

For each system there are multiple configurations used: Calibration through splitter, Direct+Cross-pole, Direct+Co-pole (S-Band). In each configuration, data is recorded with both the transfer switch disabled and enabled. Due to disk space restriction and disk write speed restrictions, data for each configuration was collected for about 10 minutes every 4 hours (including both transfer switch configuration). The algorithm used to collect data can be found in APPENDIX A2.

In the case of errors, the most common being dropped samples an overflowing samples, the step was repeated until it succeeded (up to a maximum of 3 tries). The data collection was done through a C++ script using UHD libraries for the USRP. This was based on a sample provided by Ettus Research, the manufactures of the USRP SDR. The switches for configurations were toggled through a relay that was controlled by a CURL command.

# 4. DATA PROCESSING

## 4.1 SNR of received signals

A primary method of validation of the recorded signals is looking at the SNR. The following plots show the Signal-to-Noise Ratio of the received XM signals on a linear scale. It is expected that the direct signal always has a higher SNR as compared to the reflected signal. However, on closer inspection, irregularities in the SNR of both the direct and reflected signal were observed.

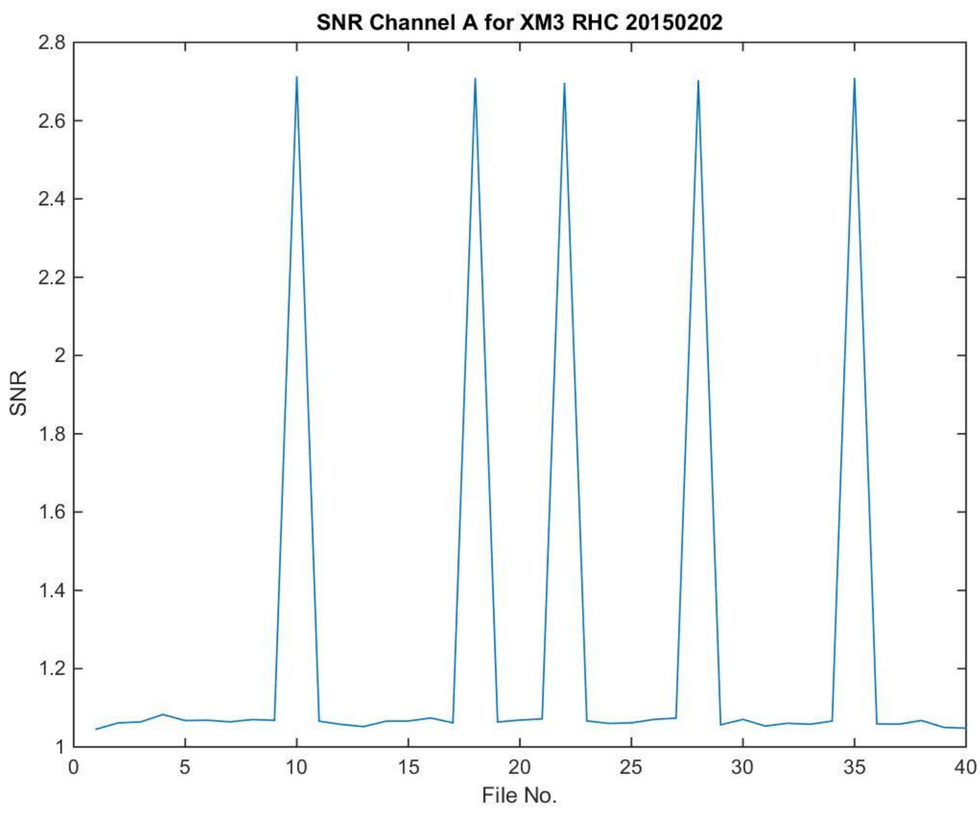


Figure 4.1 XM3 SNR for Earthview antenna over one data collection period (40 x 2sec files)

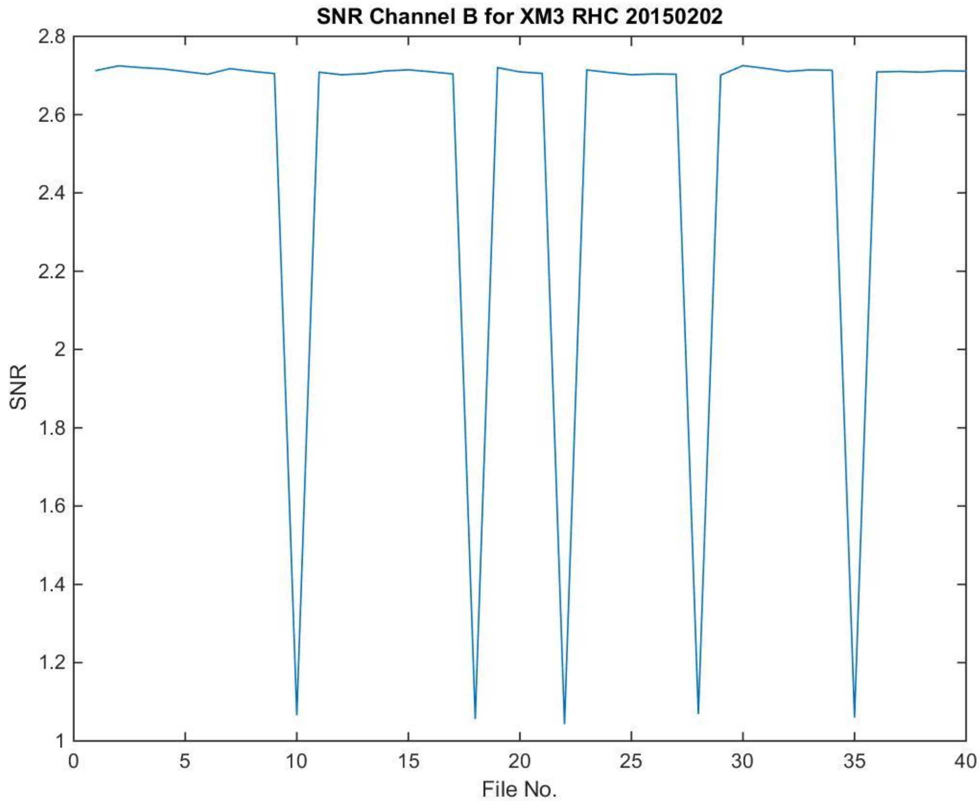


Figure 4.2 XM3 SNR for Skyview antenna over one data collection period (40 x 2sec files)

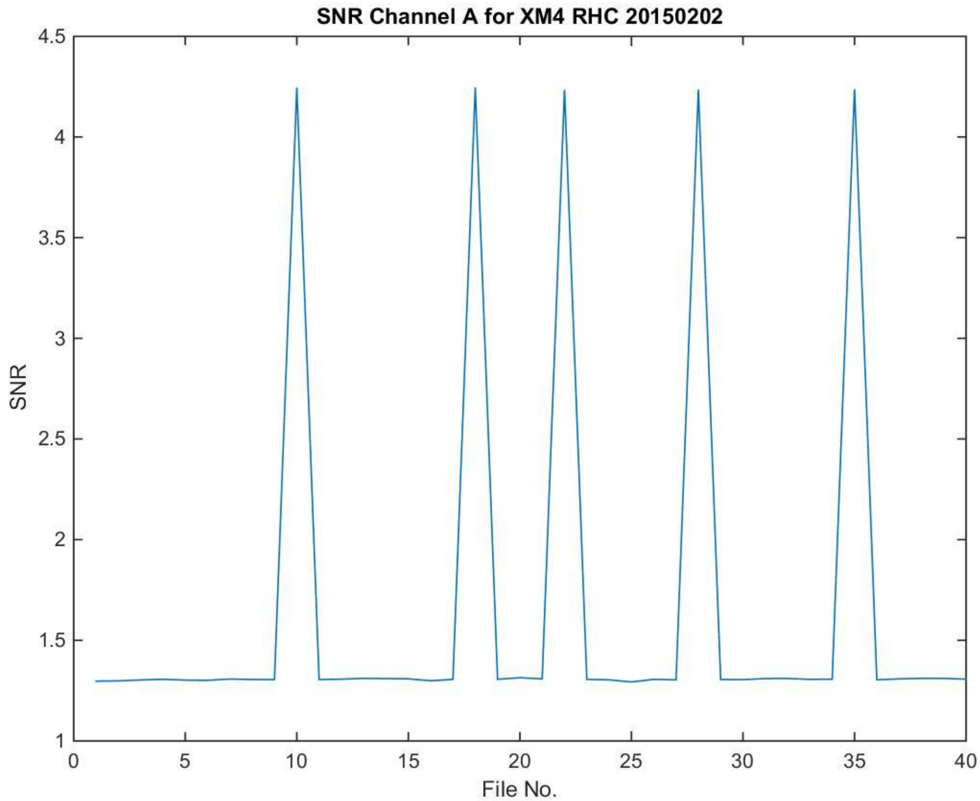


Figure 4.3 XM4 SNR for Earthview antenna over one data collection period

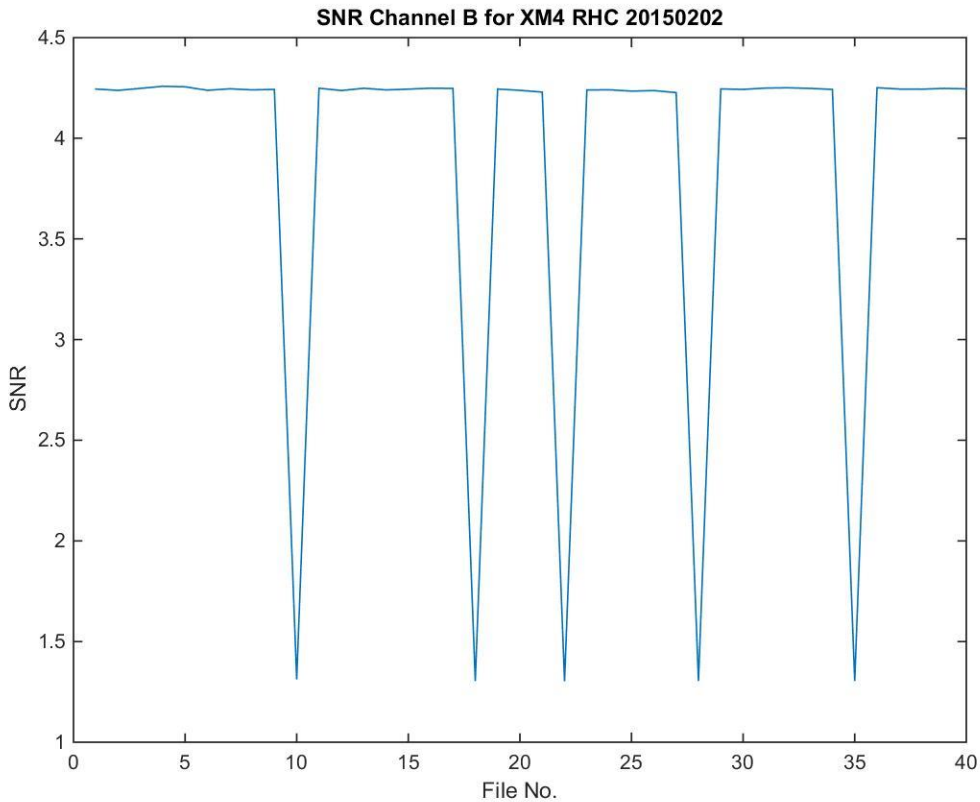


Figure 4.4 XM4 SNR for Skyview antenna over one data collection period

Spikes can be seen in the reflected signal SNRs of XM4 and XM3 as well as troughs in the direct signal. Closer observation shows that the spikes and troughs occur at the same point and the values taken by the skyview antenna at the trough is close to the normal SNR of the earthview antenna at and vice versa. This interchange of SNR between the two channels can be explained by a failure to toggle the transfer switch either due to hardware or software issues. It is expected that the transfer switch was in the opposite state as expected or in a transition state when these data sets were recorded. Since the exact situation that resulted in this phenomenon and its impact were not completely understood, a decision was made to ignore the file sets with swapped SNR values during phase and reflectivity computation.

## 4.2 Crosscorrelation of splitter calibration signals and desynchronization of channels

One of the major issues observed during this experiment was the desynchronization of the two receiving channels of the USRP while recording. This can be easily seen by looking at the delay(the point of maximum magnitude) of the cross correlation in the time domain. The following figure shows the crosscorrelation for calibration data for 02/03/14.

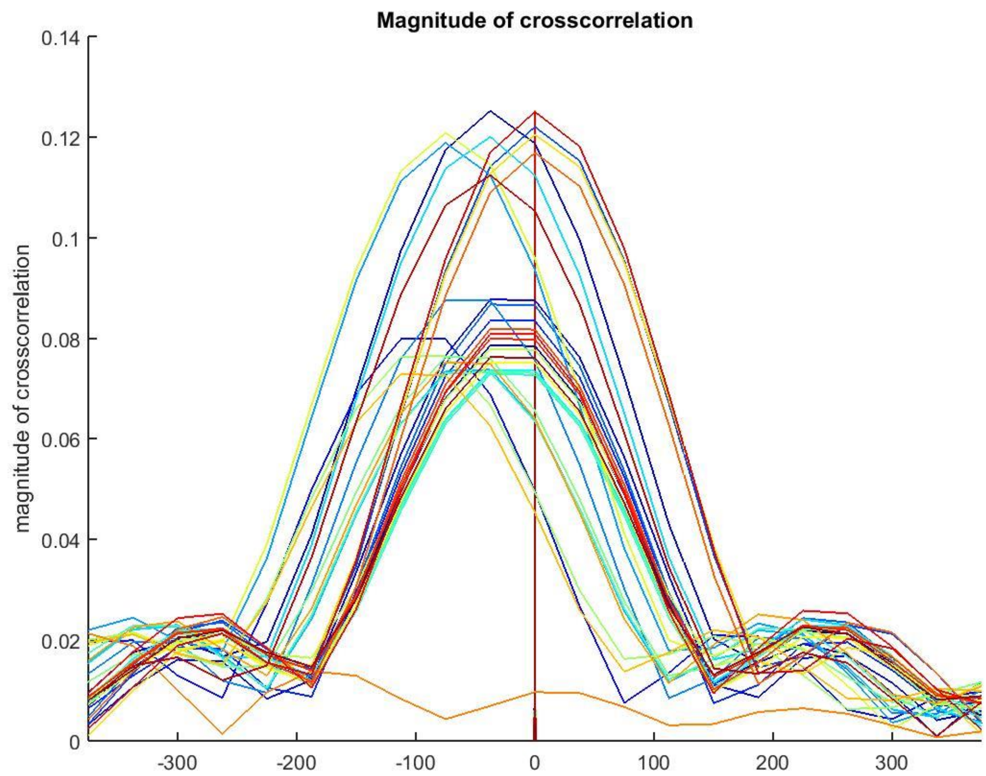


Figure 4.5 Magnitude of cross correlation vs lag in meters of skyview and earthview antenna in a 10min interval. Notice the spread of the location of the peaks

It can be seen from Figure 4.5 that the point at which the peak occurs in the cross correlation is not constant even during the span of 10min during which the data was collected. In the case of the splitter calibration configuration, the expected delay is 0 since the only difference is the two paths in the receiver. The delays observed in the cross-correlation, however, can vary by 1-2 points (each point corresponding to about 37.5m of delay) over different file sets (Channel A and Channel B) in the same time period. The delay within each file set however remains constant over the 2 second recording time. This has been seen in by other USRP B210 users in other applications and has been explained by desynchronization of the zero for each channels clock in the absence of an external time source. The issue was not an isolated case and was reproduced in a lab setting with a different USRP and computer as well as a signal generator but the using same code. The effect of the desynchronization was an ambiguity in the measured delay and phase as shown below:

$$\Delta\phi = 2\pi f_c \Delta\tau$$

$$= \frac{2\pi\Delta D}{\lambda} = 1937rad = 308.33\ cycles$$

A change in the delay by 1 sample (37m) corresponds to a slope difference of 0.82 radians over 1MHz which can result in wrapping.

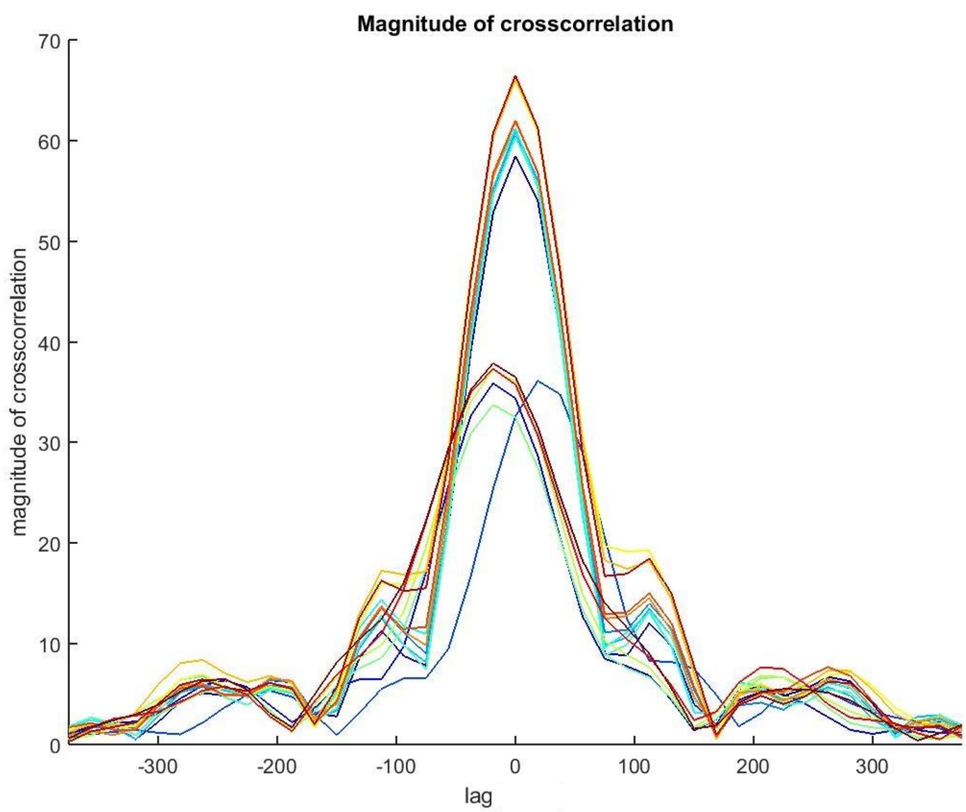


Figure 4.6 Crosscorrelation of signals from a skyview antenna split into two channels and recorded using the same setup but in the lab over 5 min. Notice the variation in the peak location.

The value of this phase change is not separable from a change in delay due to change in optical path length. Furthermore, this additional delay can be positive (if channel A is initialized before channel B) or negative (if B is initialized before A) as seen in the distributions of delay over one hour. The effect of the desynchronization, i.e. the additional delay can be modelled as a mean zero Gaussian random variable. While the phase difference for any given file set can be quite large, the averaging performed during the phase calculation gives an expected value of this additional phase as <<<0 so in an ideal case, the effect of this on a large set of data is negligible. In reality, however this is one of the major sources of error giving up to 100m of delay error in a single recording set. A second generation setup was designed using a GPSDO as an external clock which does not have this shortcoming. This will replace the current setup used in future experiment.

### 4.3 Phase Retrieval Simulation

In this section, phase/delay retrieval from a simple QPSK signal with a small artificial time delay using the above algorithm is discussed.

Let $\{d_n\}$ be a random sequence of symbols where $d_n \in \{0, 1, 2, 3\}$. Let $d(t)$ be the corresponding data stream produced from $d_n$. The QPSK encoding with a carrier frequency of $f_c$, amplitude of $A$ and a phase offset of $\phi_0$ give a signal as shown below.

$$s(t) = Ae^{i\left(\phi_0 + \frac{\pi}{2}d(t)\right)}$$

If the receiver samples at frequency $f_s$ then the model for the signal received is

$$x_D(n) = \left(s(t) + \eta_1(t)\right)_{t=nf_s}$$

$$x_R(n) = \left(s(t-\tau) + \eta_2(t)\right)_{t=nf_s}$$

Where $\eta_1(t), \eta_2(t)$ are complex Gaussian white noise with zero mean and $\tau$ is a time delay.

To retrieve the phase difference and hence, the time delay between these two signals, the algorithm presented in §2.2 is applied to these two signals. First the DFT of both signals is taken as follows, For a discrete signal $X(n)$, we define the Discrete Fourier Transform or DFT as

$$\hat{X}(k) = \sum_{n=1}^{N-1} X(n) e^{-\frac{i2\pi kn}{N}}$$

This is an approximation of the Fourier Transform with $\omega = \frac{2\pi k}{N}$

$$\hat{X}_D(\omega) = \mathcal{F}\{X_D(n)\}$$

$$\hat{X}_R(\omega) = \mathcal{F}\{X_R(n)\}$$

We now have from §2.2

$$\omega_c \tau = \phi = \underset{\theta}{\operatorname{argmin}} \left| \gamma(\omega) - \frac{\theta\omega}{\omega_c} \right|, \omega \in B$$

Since signal is affected by noise we use a moving average on $\gamma(\omega)$ before solving the least squares minimization problem.

An analysis of the expected error from the method can be performed from the simulation by observing $\hat{\tau} - \tau$ where $\hat{\tau}$ is the estimate of the delay from the simulation and $\tau$ is the delay inputted into the simulation. The results of this analysis can be seen below in Figure 4.7. Delays from 4e-8 to 2e-7 were analyzed to look at error estimation within delays observed in actual data. This estimated error at delays observed, however is smaller than the standard deviation.

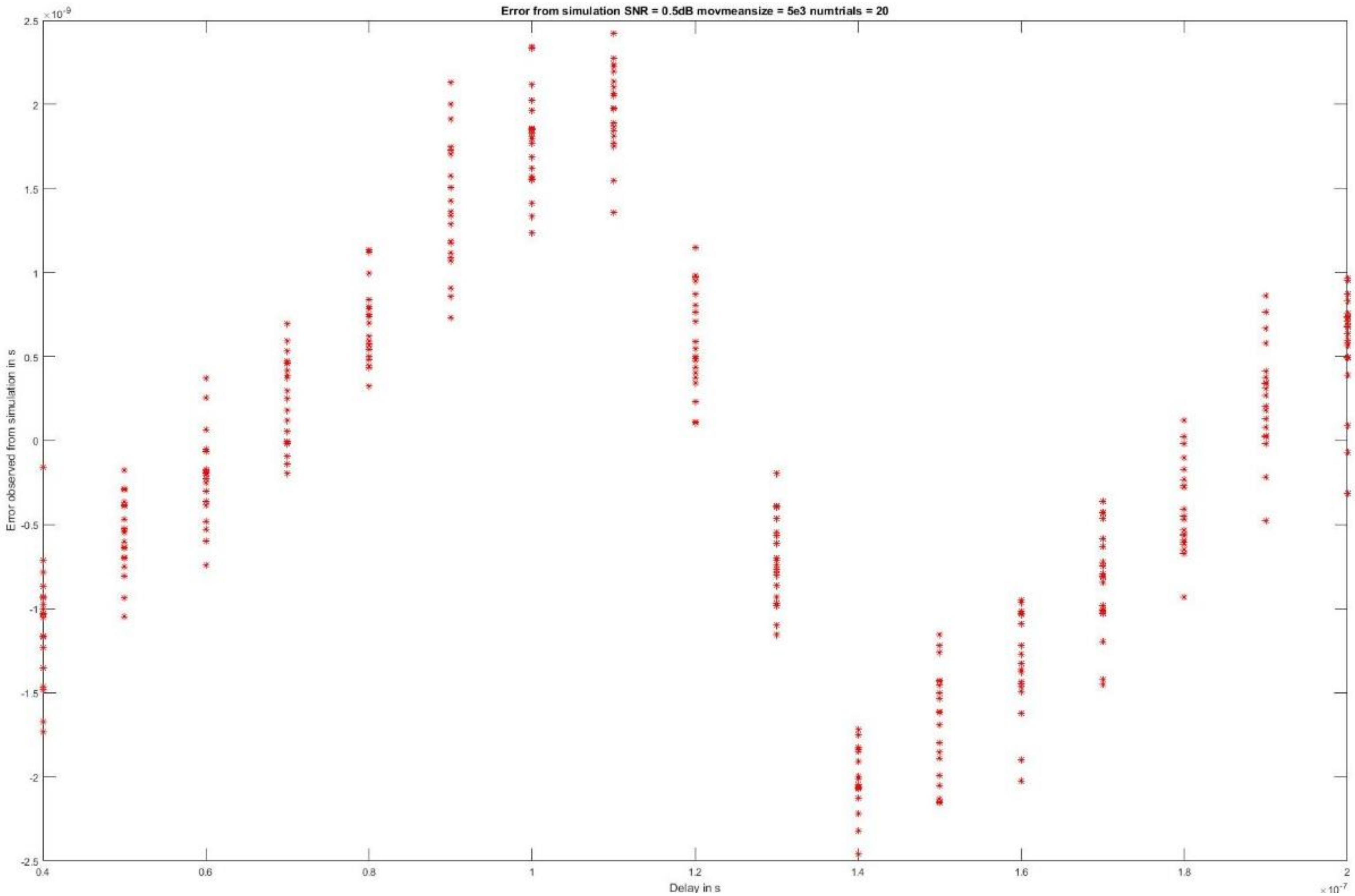


Figure 4.7 Error estimation from simulation vs delay

# 5. RESULTS

## 5.1 Phase results (vs model)

The snow depth trend across the months that data was collected can be seen in

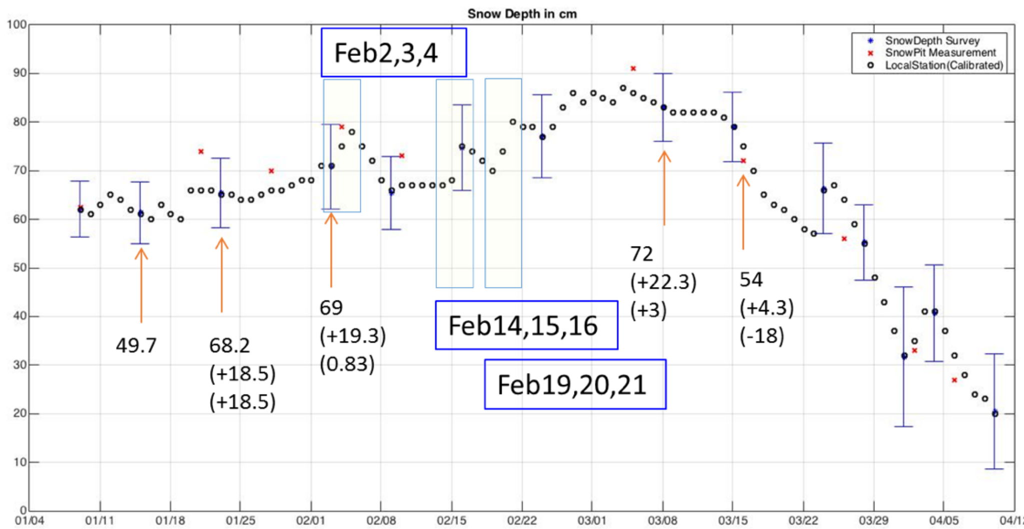


Figure 5.1 Snow depth change during experiment

The following figure shows the computed phase change for XM3 and XM4 along with the phase change predicted by the model [12] [21] [22] [12].

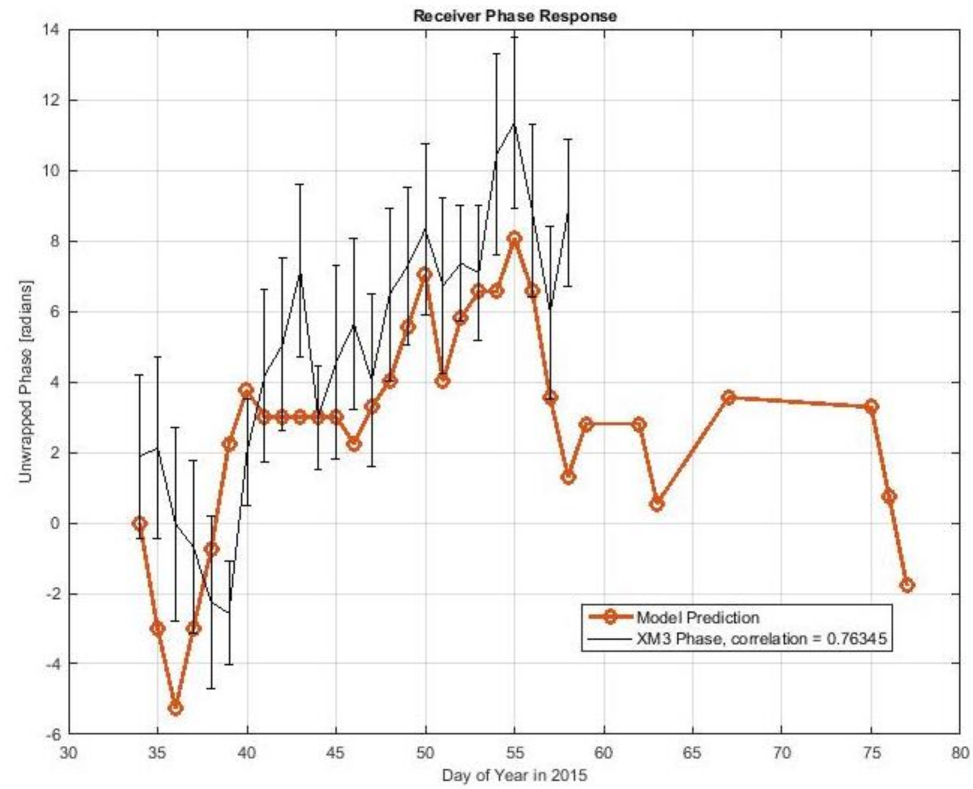


Figure 5.2 XM3 phase and modelled phase [21] during the month of February 2015

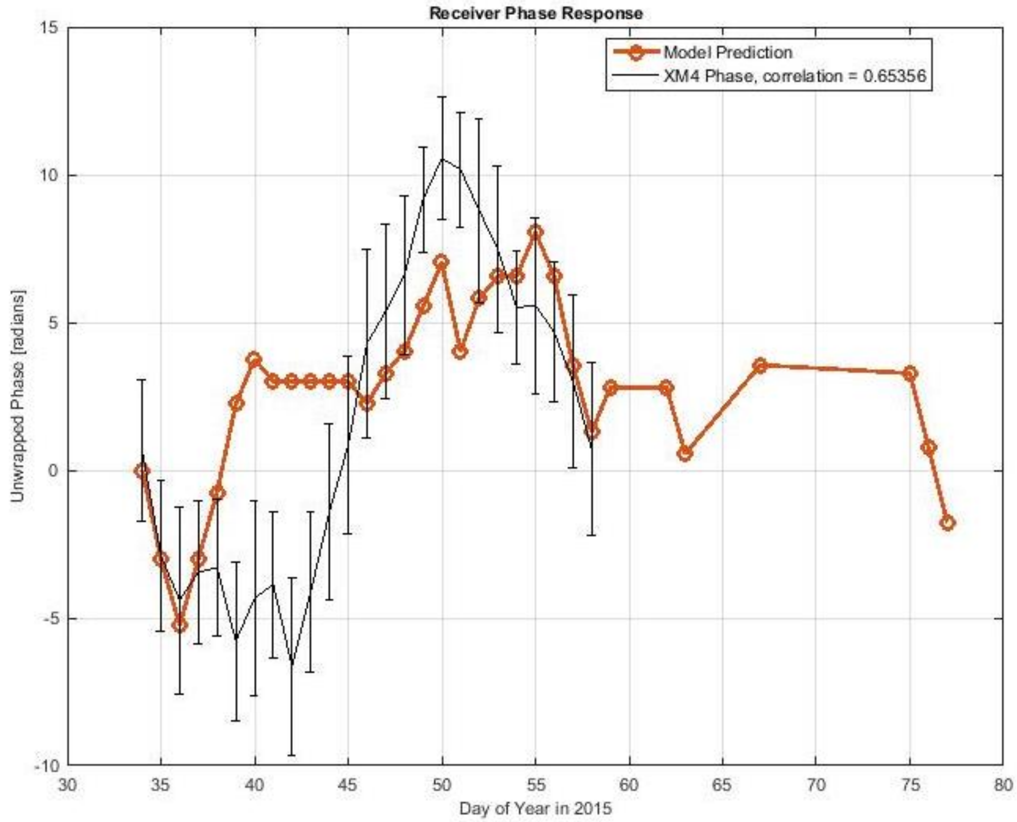


Figure 5.3 XM4 phase and modelled phase [21] during the month of February 2015

From Figure 5.2 and Figure 5.3 we can see that the computed phase roughly follows the modelled phase with some errors. XM4 shows more deviation from the model than XM3. This may be a result of different specular reflection points for XM3 and XM4. Additionally, this may be a result of poor phase unwrapping in XM4 phase retrieval. Error bars shown are from the standard deviation of the phase calculated as shown in 2.5.

## 5.2 Reflectivity Results (vs air temperature/ soil temperature)

The typical reflectivity variation across a single day can be seen for the span of Feb 3-11 in Figure 5.4.

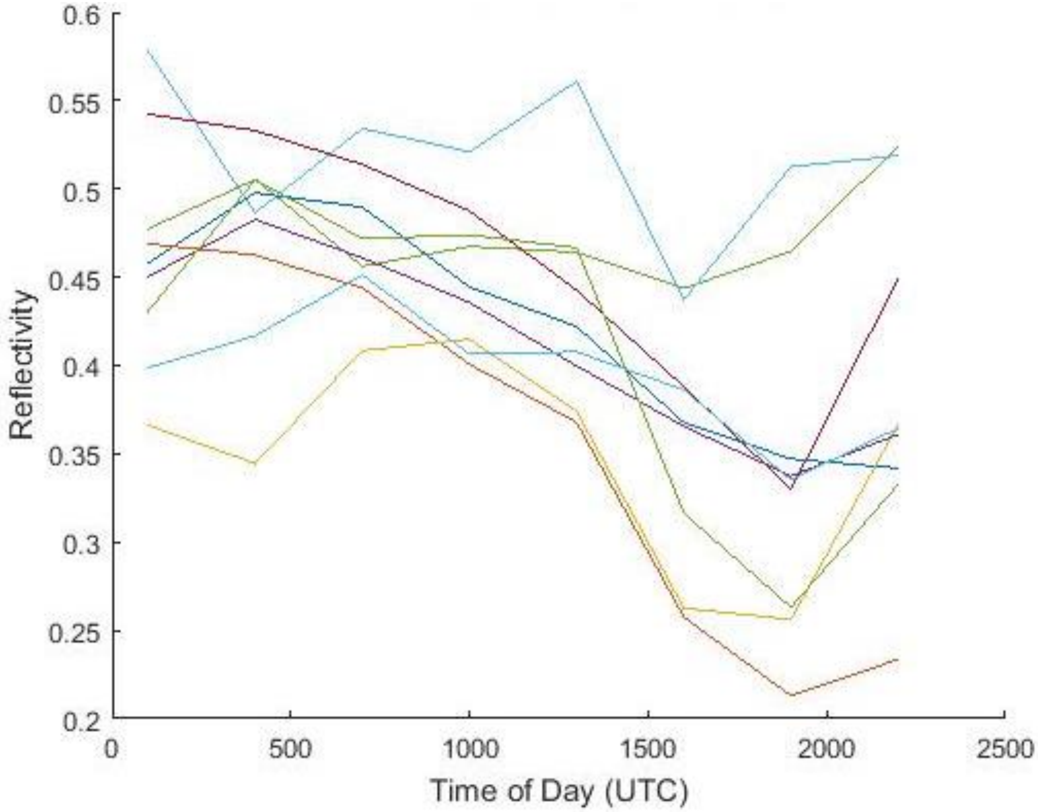


Figure 5.4 Diurnal variation of reflectivity for XM3 for Feb 3-11

A cyclic diurnal trend can be seen from Figure 5.4. This needs to be accounted for while looking at long term trends across the course of multiple days. The cyclical component can be filtered out from the long term trend (over the course of multiple days) using various methods. The method used here involves the use of the Hodrick-Prescott (HP) filter [23]. The HP filter is often seen in macroeconomics to separate the cyclical component from the long term trend in data. For this experiment, the time series contains 8 data points per day or 8 data points per cycle. Consequently, a smoothing factor of $6400 = (8)^2 * 100$ is used. The least squares problem solved by the HP filter is

$$\min_{\tau}\left(\sum_{i=1}^{N}(y_i - \tau_i)^2 + \lambda\sum_{i=2}^{N-1}\big((\tau_{i+1} - \tau_i) - (\tau_i - \tau_{i-1})\big)\right)$$

Where $\lambda$ is the smoothing parameter.

The following figure shows the estimated XM3 reflectivity vs time for different time periods in January, February, and March along with the trend component of the HP filter.

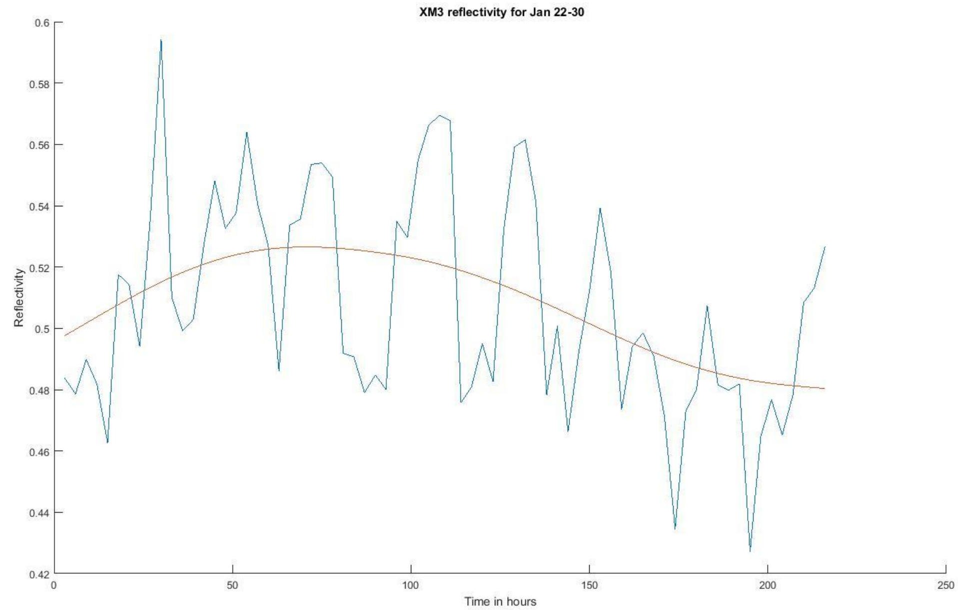


Figure 5.5 XM3 reflectivity + trend for Jan 22-30

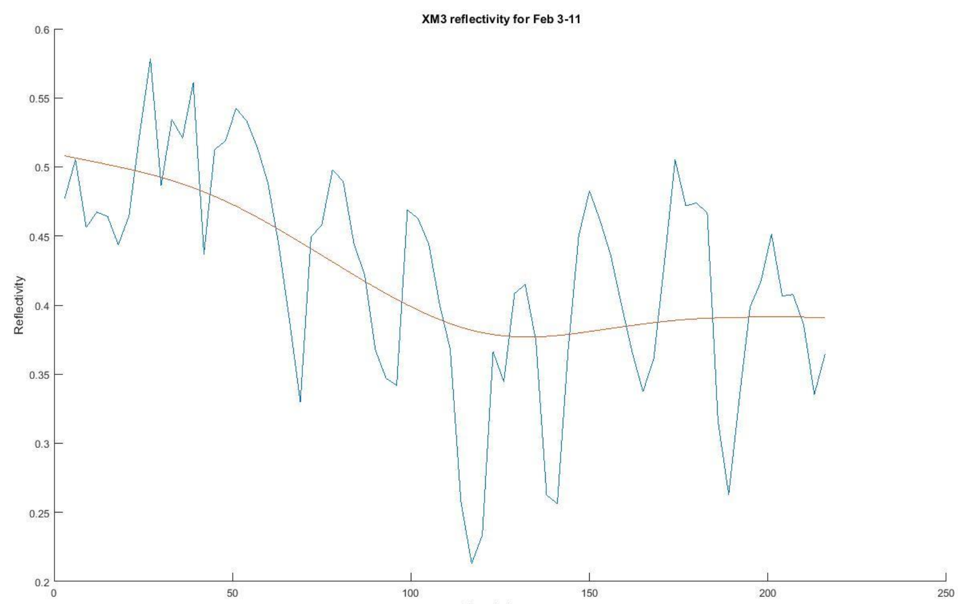


Figure 5.6 XM3 reflectivity + trend for Feb 3-11

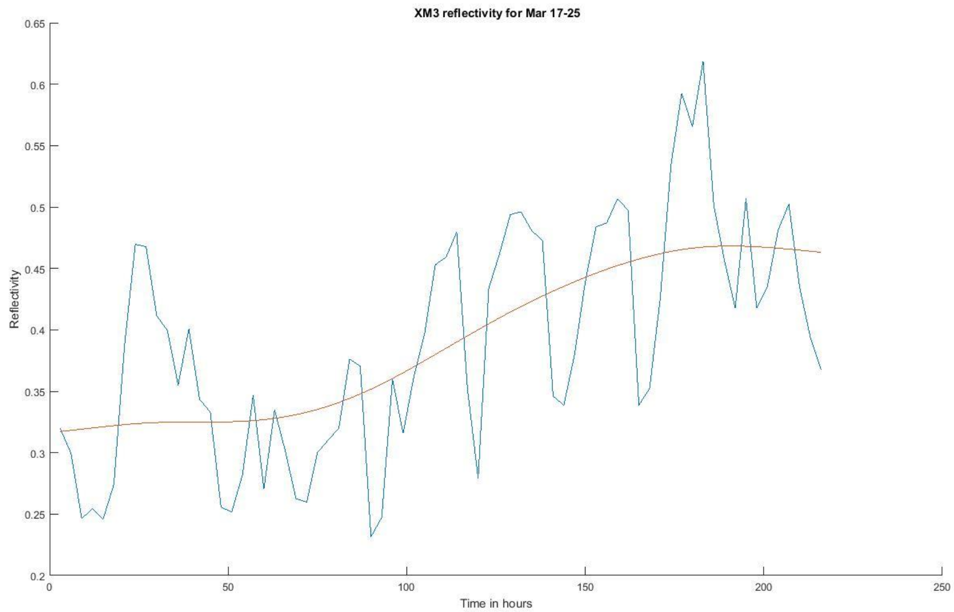


Figure 5.7 XM3 reflectivity + trend for Mar 17-25

For comparison, the air temperature and trends for the same periods are presented below.

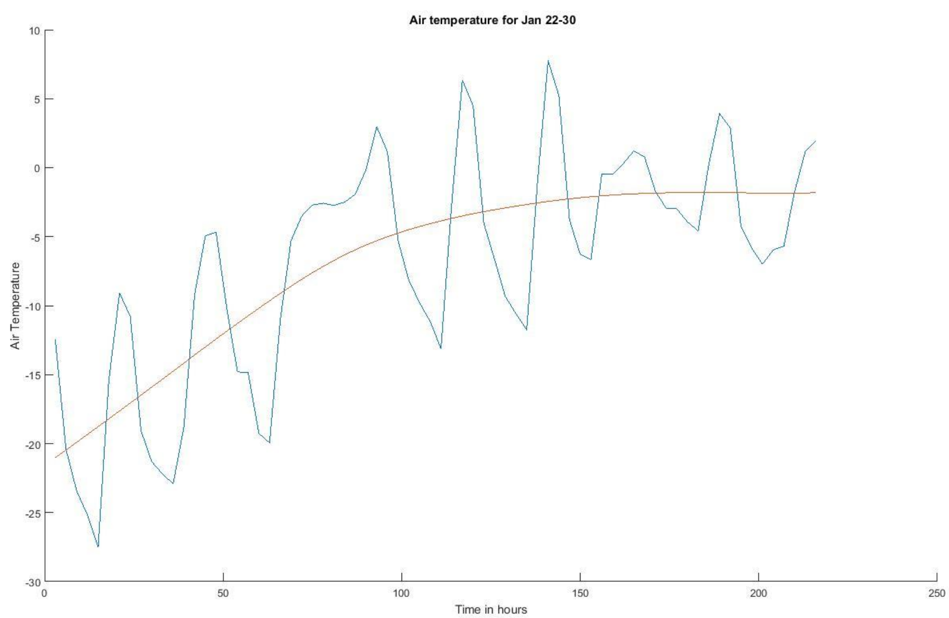


Figure 5.8 Air Temperature + trend for Jan 22-30

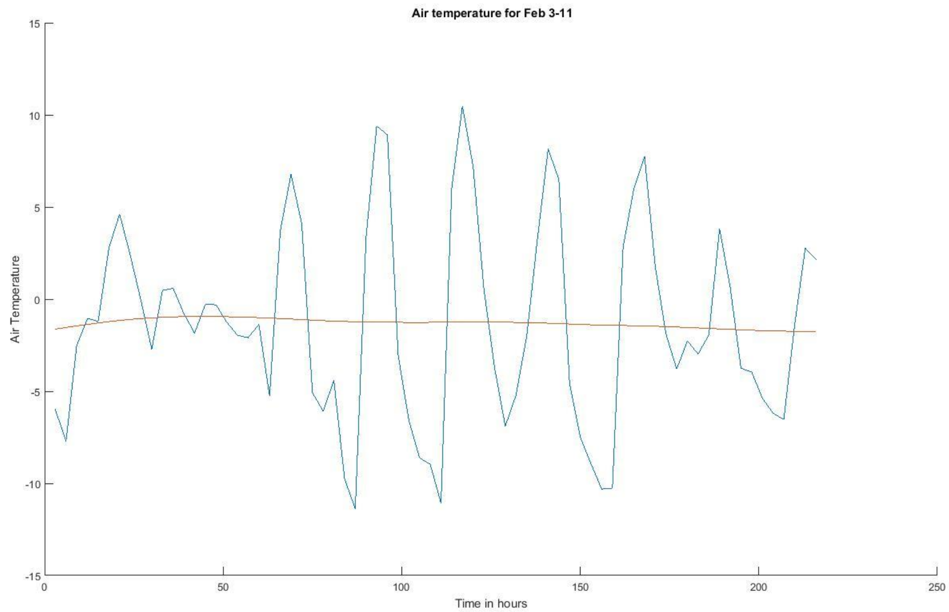


Figure 5.9 Air temperature + trend for Feb 3-11

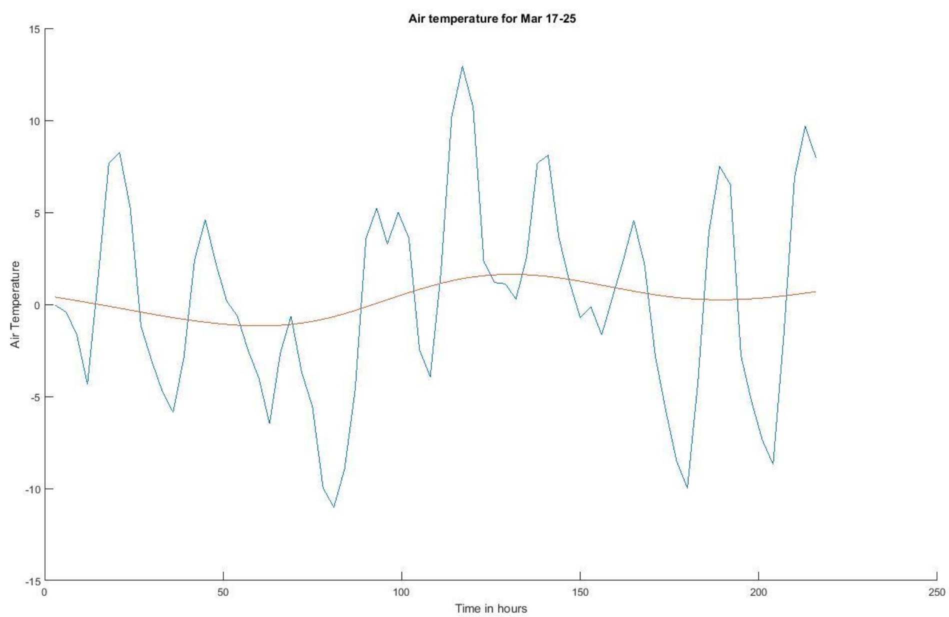


Figure 5.10 Air temperature + trend for Mar 17-25

In general an inverse correlation can be seen between reflectivity (including the cyclical component) and the air temperature. However dry snow has a reflection coefficient close to 0 and ice has a reflection coefficient of 0.99 [24] [13] [25], the formation and thawing of ice layers (usually when air temperature is $\sim 0^0 C$ ) can make this relationship more complicated than a simple inverse correlation. Ice layers were observed in the snow during in-situ measurements made at the experiment site in Fraser CO and must be taken into account. This requires a more complicated model to assess the relationship between reflectivity and measured temperature that accounts for this ice layer.

# 6. CONCLUSION

## 6.1 Conclusion

In this thesis, a method of remote sensing of snow using bistatic radar reflectometry is discussed. A field campaign is designed to explore this method and deployed in Fraser, CO from January 2015 to April 2015. S band signals reflected off the air-snow-soil system are recorded and compared to direct S-band signals recorded simultaneously. The phase measured through this method is compared to phase from a forward model based on Snow Water Equivalent (SWE) measured through in-situ measurements. The measured phase is found to be correlated with the forward model with a correlation coefficient of 0.76 for XM3 and 0.65 for XM4. The error in this estimation of phase is calculated using the standard deviation of a wrapped normal distribution and was found to be 2.55 rad. Additional, the reflectivity was found for the duration of the campaign and compared to air temperature. However no conclusive relationship was observed. This may be a result of melting and freezing of snow layers during the experiment.

## 6.2 Future Work

There are several steps that can be taken in the future to improve the results from this experiment as well as additional experiments that can be performed and compared to this method. To start with, the results from the P band data collected in this experiment (see APPENDIX A1) can be computed and compared with the S band results shown here. A similar experiment using L band signals such as GPS would be very valuable in understanding how carrier frequency and the associated phase wrapping affects SWE retrieval through phase measurements. Additionally, SWE retrieval can be performed using other known remote sensing methods such as GPS interferometric reflectometry or radiometry should be performed simultaneously and the results compared with the reflectometry method discussed here. Improved signal processing techniques can also be used to improve the performance and the accuracy of the phase retrieval using the algorithm described in this thesis.

# APPENDIX A1. P BAND SYSTEM

The design of the experiment includes applying the reflectometry model discussed in Chapter 2 to P band signals using signals from UHF Follow On satellites as well. These results are to be compared with the S band results and used in conjunction to improve the accuracy of the results. While the P band data was collected as planned a major problem developed which resulted in the S band data processing being prioritized over the P band data.

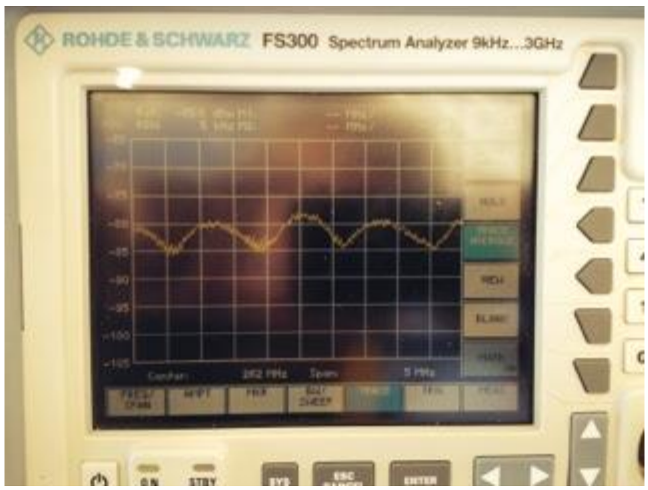


Figure A1.6.1 P Band interference observed at Fraser CO

While looking at the power spectral density for the P Band system after deployment, a 1 MHz bandwidth recurring interference was observed (Figure A1.6.1) that was not observed during ground tests of the Yagi antennas at Purdue University. After various field testing during and after the campaign, the cause of this interference was determined to be the presence of the relay used for the switches in the vicinity of the antenna and amplifier. This can be seen clearly in the figure shown below. Further testing done back at Purdue University with a similar antenna-amplifier-relay setup showed that the interference was a result of the presence of the powered relay near the amplifier (Figure A1.6.2), but was further amplified when the P Band amplifier and the relay had a common power source as was the case in the field campaign.

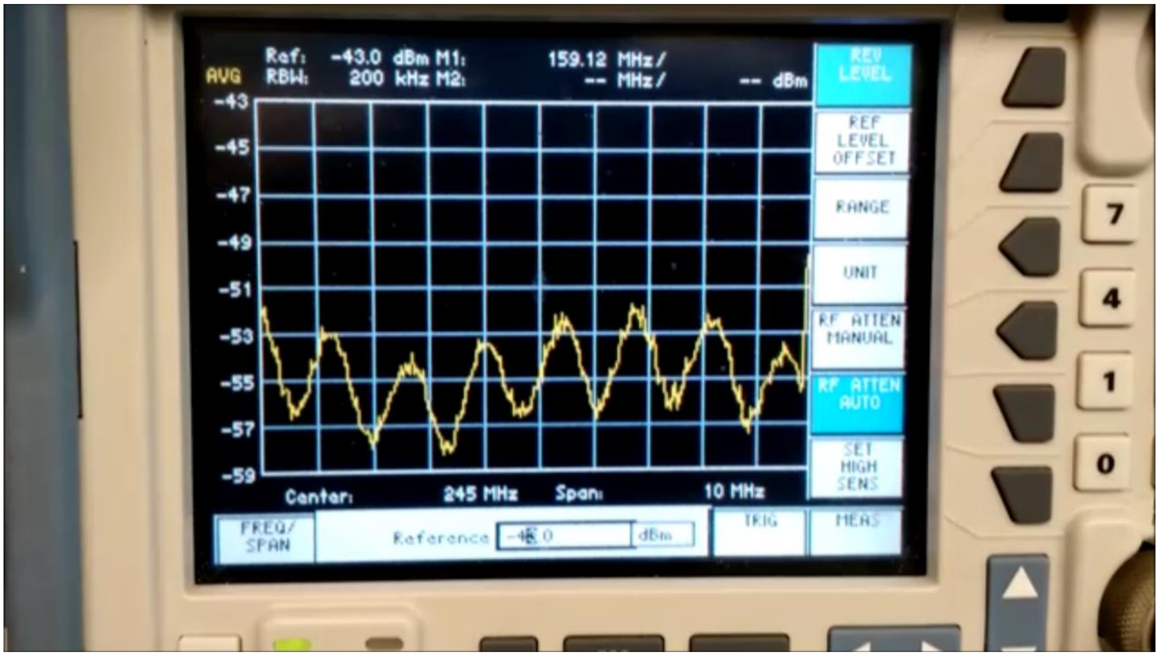


Figure A1.6.2 Interference reproduced in the lab (relay turned on)

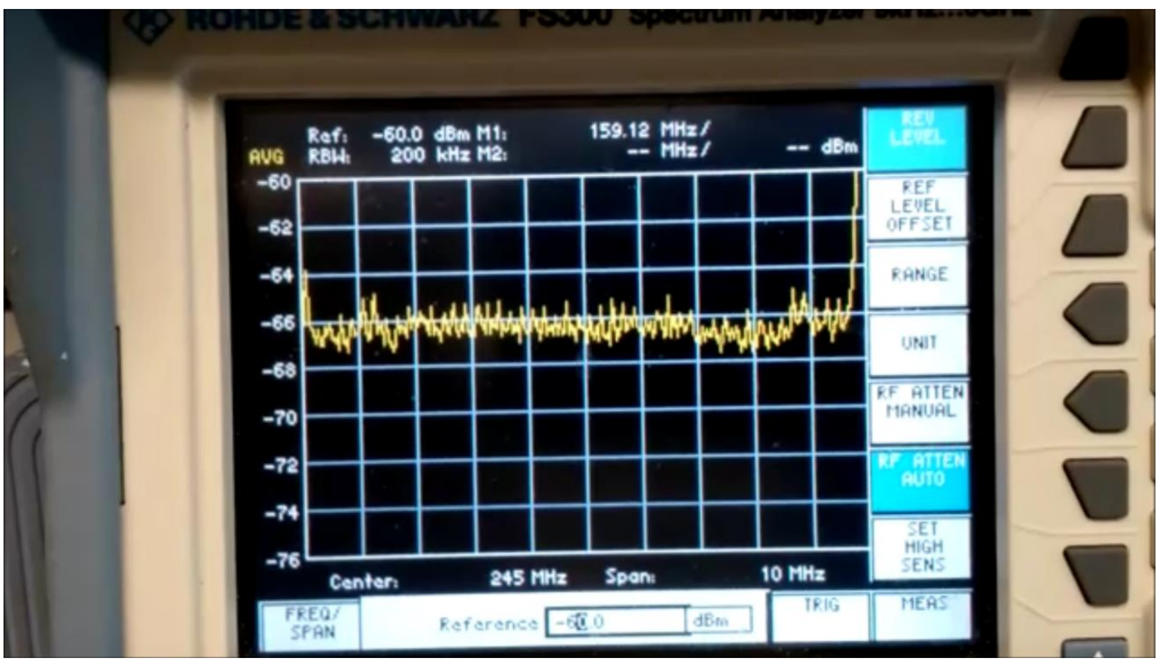


Figure A1.6.3 Interference reproduced in the lab (relay turned off)

# APPENDIX A2. DATA COLLECTION ALGORITHM

A typical loop (with no errors) for S-Band looked as follows:

1) Check for USRP connection
2) Switch to Splitter configuration
3) Collect Data for Splitter configuration (2 sec)
    3a. Collect Data for Splitter configuration (2 sec)
    3b. Activate Transfer Switch (TS)
    3c. Collect Data for Splitter configuration + TS (2 sec)
    3d. Reset Transfer Switch
4) Switch to Cross-pole configuration
5) Collect Data for Cross-pole configuration (2 sec)
    5a. Collect Data for Cross-pole configuration (2 sec)
    5b. Activate Transfer Switch
    5c. Collect Data for Cross-pole configuration + TS (2 sec)
    5d. Reset Transfer Switch
6) Switch to Co-pole Configuration
7) Collect Data for Co-pole configuration (2 sec)
    7a. Collect Data for Co-pole configuration (2 sec)
    7b. Activate Transfer Switch
    7c. Collect Data for Co-pole configuration + TS (2 sec)
    7d. Reset Transfer Switch
8) Repeat steps 2-7 until 10 minutes of data for each configuration have been collected.
9) Sleep for 3.5 hours and go to step 1.

# APPENDIX A3. XM DIGITAL FILTERS

The two XM bands correspond to two different satellites are filtered out using different FIR filters during data processing to isolate signals from the different specular points. The frequency response of each filter juxtaposed on the spectrum of collected data is shown below.

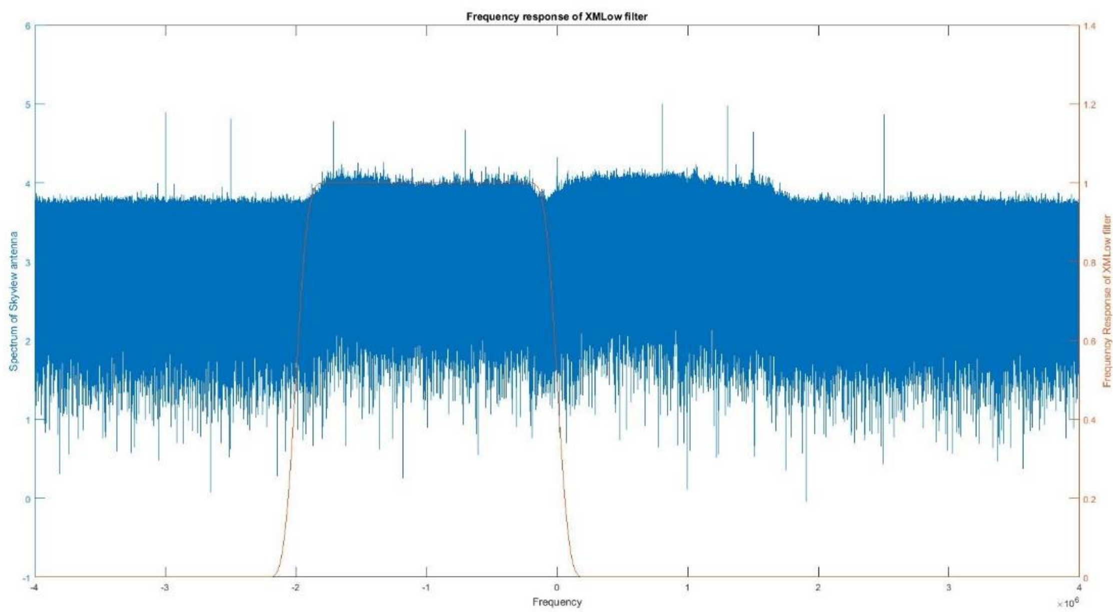


Figure A2.1 Frequency Response of XMLow filter

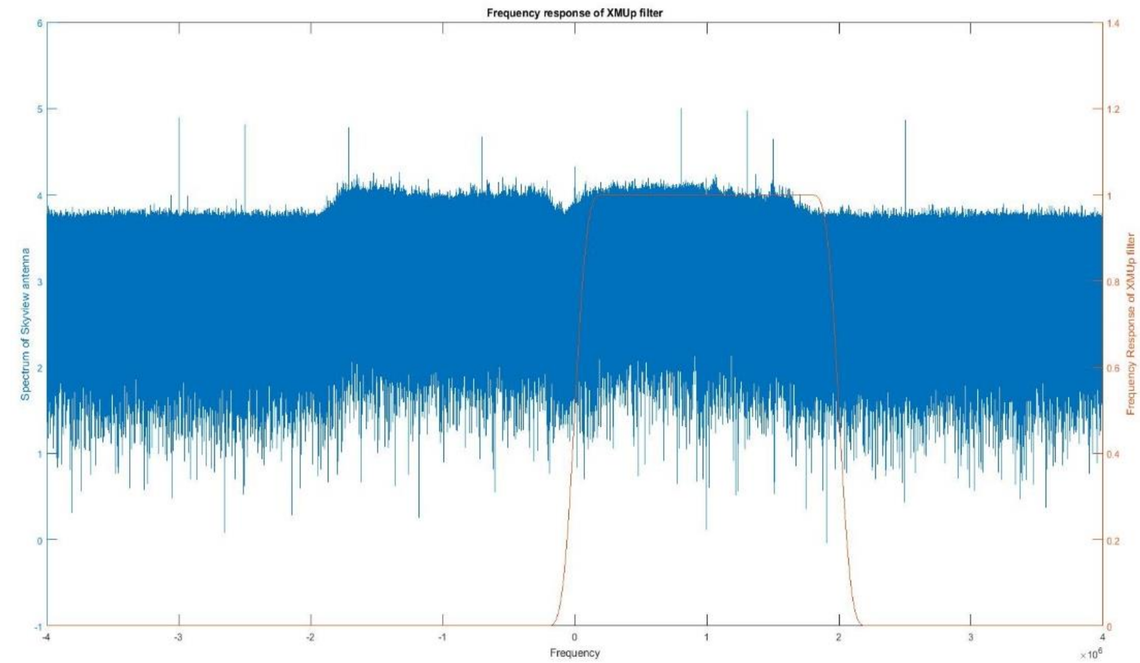


Figure A2.2 Frequency Response of XMUp Filter

The appropriate filter is selected and applied to both the direct and reflected signal before the signals are cross correlated. Since the same filter is used on both signals, there is no change in phase delay estimation using the cross correlation in the frequency domain due to the application of the filter

# APPENDIX A4. DATA MANAGEMENT

One of the major issues faced during campaign was the management of the large amounts of data collected over the course of 4 months for both the P band and S Band systems. At the rate of approximately 2.5 TB per week this totaled approximately 25TB. This data had to be moved from the experiment site in Fraser, CO to Purdue University, West Lafayette, IN on a biweekly basis. Once at Purdue University, a local working backup as well as a long term backup of the data needed to be established. A local working copy was established on a Drobo while a long term backup was made using the university tape drive system.

Data recorded was stored in a generic DAT file format for ease of access on both Windows and Linux machines. The file names included identifiers for the date and time of recording as well as flags indicating the configuration of the system during the recording.

While the system used was acceptable for this campaign, a better management plan for transferring data from the data collection PC to external storage with minimum downtime needs to be established. Intermediate products of data that can be used for data processing while taking up reduced storage space also need to be identified.

# APPENDIX A5. XM CO-POLE RECORDING

The field campaign planned for both co-pole and cross-pole reflected signals to be collected. However Early on in the field campaign, the code was inadvertently modified during field testing and did not always send the command to switch to the LHCP reflected antenna during the appropriate phase of data collection. Furthermore, a hardware defect was found in the set up where the earth-view LHCP XM antenna was not properly connected. As a result, the earth-view LHCP data obtained was deemed invalid for this campaign. Further work needs to be done to design a system with the capability to verify that the correct switches have been triggered and a reasonable signal is being recorded.

# REFERENCES


[1] T. Barnett, J. Adam and D. Lettenmaier, "Potential impacts of a warming climate on water availability in snow-dominated regions," *Nature*, pp. 303-308, 2005.

[2] R. Shah, J. L. Garrison and M. S. Grant, "Demonstration of bistatic radar for ocean remote sensing using communication satellite signals," *Geoscience and Remote Sensing Letters*, vol. 4, no. 9, pp. 619-623, 2012.

[3] R. A. e. a. Anthes, "Earth Science and Applications from Space: National Imperatives for the Next Decade and Beyond," Space Studies Board, National Research Council, Washington DC, 2007.

[4] A. Nolin, "Recent advances in remote sensing of seasonal snow," *Journal of Glaciology*, pp. 1141-1150, 2010.

[5] H. Rott, S. Yueh, D. Cline, C. Duguay, R. Essery, C. Haas and A. Thompson, "Cold Regions Hydrology High-Resolution Observatory for Snow and Cold Land Processes," *Proceedings of the IEEE*, pp. 752-765, 2010.

[6] X. Xu and S. (. Yueh, ".Multi-Frequency Bistatic Reflectometry over terrestrial snow cover Using Signals of Opportunity.," NASA Jet Propulsion Laboratory.

[7] A. Chang, J. Foster, D. Hall, A. Rango and B. Hartline, "Snow water equivalent estimation by microwave radiometry," *Cold Regions Science and Technology*, pp. 259-267, 1982.

[8] E. Cardellach, F. Fabra, A. Rius, S. Pettinato and S. D'Addio, "Characterization of dry-snow sub-structure using GNSS reflected signals," *Remote Sensing of Environment*, vol. 124, pp. 122-134, 2012.

[9] K. Larson, "GPS Interferometric Reflectometry: Applications to Surface Soil Moisture, Snow Depth, and Vegetation Water Content in the Western United States," *WIREs Water*, vol. 3, pp. 775-787, 2016.

[10] E. Gutmann, K. M. Larson, M. Williams, F. Nievinski and V. Zavorotny, "Snow measurement by GPS interferometric reflectometry: an evaluation at Niwot Ridge, Colorado," *Hydrologic Processes,* vol. 26, pp. 2951-2961, 2012.

[11] McCreight, E. Small and K. Larson, "Snow Depth, Density, and SWE estimates Derived from GPS Reflection Data: Validation in the Western U.S.," *Water Resources Research,* vol. 50, 2014.

[12] S. Yueh, X. Xu, R. Shah, Y. Kim, J. Garrison, A. Komanduru and K. Elder, "Remote Sensing of Snow Water Equivalent Using Radio Signals of Opportunity: Theoretical Modeling," *TBD,* 2016.

[13] F. T. Ulaby, R. K. Moore and A. K. Fung, Microwave Remote Sensing: Active and Passive, Volume II: Radar Remote Sensing and Surface Scattering and Emission Theory, Artech House Publishers, 1986.

[14] "XM Satellite Technology," Rohde & Schwarz GmbH & Co. KG, 2016. [Online]. Available: https://www.rohde-schwarz.com/us/technologies/satellite-broadcast/xm-satellite/xm-satellite-technology/xm-satellite-technology_55613.html. [Accessed 25 November 2016].

[15] "XM 4," LyngSat, [Online]. Available: http://www.lyngsat.com/XM-4.html. [Accessed 25 November 2016].

[16] R. Shah., "Analysis of the correlation properties of digital satellite signals and their applicability in bistatic remote sensing.," *ProQuest Dissertations and Theses,* p. 156, 2010.

[17] "Satellite Space Applications Accepted for Filing," FCC US, 9 June 2006. [Online]. Available: https://apps.fcc.gov/edocs_public/attachmatch/DOC-265875A1.pdf. [Accessed 25 November 2016].

[18] K. Mardia and P. E. Jupp, Directional Statistics, Wiley, 1999.

[19] "XM or SIRIUS Radio Antenna, P/N: 3X23X-XX-X," Antcom, [Online]. Available: http://www.antcom.com/documents/catalogs/Page/3X23X-XX-X_XMorSIRIUSAntennas.pdf. [Accessed 8 December 2016].

[20] "Universal Software Radio Peripheral B200/B210 Bus Series.," Ettus Research, [Online]. Available: http://www.ettus.com/content/files/b200-b210_spec_sheet.pdf. [Accessed 25 November 2016].

[21] R. Shah, X. Xu, S. Yueh, Y. Kim, J. Garrison, A. Komanduru and K. Elder, "Remote Sensing of Snow Water Equivalent Using Radio Signals of Opportunity: Experimental Demonstration," *TBD*, 2016.

[22] T. Leung, P. Jin, L. Ding, L. Zhongxin, D. W. Cline and T. Yunhua, "Modeling Active Microwave Remote Sensing of Snow Using Dense Media Radiative Transfer (DMRT) Theory With Multiple-Scattering Effects," *IEEE Transactions on Geoscience and Remote Sensing,* vol. 45, pp. 990-1004, 2007.

[23] R. Hodrick and E. C. Prescott, "Postwar U.S. Business Cycles: An Empirical Investigation," *Journal of Money, Credit, and Banking,* vol. 29, p. 1–16, 1997.

[24] F. T. Ulaby and W. H. Stiles, "The active and passive microwave response to snow parameters. 2. Water equivalent of dry snow," *J. Geophys. Res.,* vol. 85, pp. 1045-1049, 1980.

[25] M. Hallikainen, F. Ulaby and T. Deventer, "Extinction Behavior of Dry Snow in the 18-to 90-GHz Range," *IEEE Transactions on Geoscience and Remote Sensing,* pp. 737-745, 1987.